Research Square

Preprints are preliminary reports that have not undergone peer review.
They should not be considered conclusive, used to inform clinical practice,
or referenced by the media as validated information.

Messinian Atlantic-Mediterranean gateway restriction modified overflow and reshaped Atlantic deep waters

F.J. Hernández-Molina

jhbaiona@gmail.com

Spanish Research Council (CSIC) https://orcid.org/0000-0002-7483-1443

F.J. Sierro

Universidad de Salamanca

A. Laake

slb

D. Duarte

Spanish Research Council (CSIC)

Zhi Lin Ng

Sun Yat-sen University https://orcid.org/0000-0003-2943-2133

Fadl Raad

CNRS https://orcid.org/0000-0002-7143-2420

S. Yin

Second Institute of Oceanography, Ministry of Natural Resources of China

M. Teixeira

Spanish Research Council (CSIC)

C. Serie

Vår Energi ASA

E. Llave

Instituto Geológico y Minero de España

S. Ledesma

Trinity Energy Storage SL

J. Fedele

ExxonMobil Upstream Research Company

A. Naveira Garabato

University of Southampton

A. Piola

Universidad de Buenos Aires

M. Ron Martin

REPSOL, S.A

A. Arnaiz

REPSOL, S.A

E. Ducassou

University of Bordeaux

T. Williams

University of South Florida

R. Flecker

University of Bristol

Article

Keywords:

Posted Date: November 25th, 2026

DOI: https://doi.org/10.21203/rs.3.rs-11084393/v1

License: This work is licensed under a Creative Commons Attribution 4.0 International License.
Read Full License

Additional Declarations: There is **NO** Competing Interest.

Messinian Atlantic-Mediterranean gateway restriction modified overflow and reshaped Atlantic deep waters

F.J. Hernández-Molina[1*], F.J. Sierro[2], A. Laake[3], D. Duarte[1], Z.L. Ng[4], F. Raad[5], S. Yin[6], M. Teixeira[1], C. Serie[7], E. Llave[8], S. Ledesma[9], J. Fedele[10], A. Naveira-Garabato[11], A. Piola[12], M. Ron Martin[13], A. Arnaiz[13], E. Ducassou[14], T. Williams[15], R. Flecker[16]

[1] Andalusian Earth Sciences Institute (IACT-CSIC); Avda. de Las Palmeras, 4. 18100. Armilla, Granada, Spain.

[2] Dpto. de Geología, Univ. de Salamanca; 37008 Salamanca, Spain

[3] slb, Germany

[4] School of Marine Sciences, Sun Yat-Sen University, China

[5] Géosciences Montpellier, CNRS, Université de Montpellier; Place E. Bataillon, 34095 Montpellier Cedex 05, France

[6] Second Institute of Oceanography; Hangzhou 310012, China

[7] Vår Energi ASA; Pb 101, 4068 Stavanger, Norway

[8] Instituto Geológico y Minero de España (IGME-CSIC); 28003 Madrid, Spain

[9] Trinity Energy Storage SL.; 28050 Madrid, Spain

[10] GNO-E&NV ExxonMobil Corporation; Houston, TX, USA

[11] Univ. Southampton; Southampton, SO17 1BJ, United Kingdom

[12] FCEN, Univ. Buenos Aires & CONICET/UBA/CNRS/IRD; Buenos Aires, Argentina

[13] REPSOL S.A.; 28045 Madrid, Spain

[14] Univ. Bordeaux, EPOC; UMR CNRS 5805, France

[15] Univ. South Florida; Tampa, FL 33620, USA

[16] Univ. Bristol, School of Geographical Sciences; Bristol, UK

*Corresponding author. Email: fj.h@csic.es

Abstract

Ocean gateway changes alter global ocean circulation. The Messinian Salinity Crisis (~5.97–5.33 Ma), during which the Mediterranean Sea became highly saline, provides a natural test of such change, yet its impact on Mediterranean-Atlantic exchange remains unresolved for lack of evidence outside the Mediterranean. Here we present the first deep-marine record from the Atlantic margin, tracing Mediterranean Outflow evolution before and during the crisis and reconstructing gateway dynamics and their interbasin consequences. We identify seven phases: weak overflow (8–6.4 Ma); which became increasingly dense before (6.4-5.97 Ma) and during initial evaporite precipitation (5.97-5.78 Ma), peaking at the crisis' acme (~5.78-5.6 Ma); abrupt reduction at ~5.60 Ma; cessation by ~5.55 Ma; and no overflow (5.55-5.33) Ma. We conclude that, in the late Messinian, dense Mediterranean waters penetrated deeply into the Atlantic Ocean's abyss, exerting a basin-wide influence on the density structure, overturning circulation, upwellings and biogeochemical cycling.

INTRODUCTION

Earth's transition toward modern icehouse conditions during the middle-late Miocene (~14.0–5.33 Ma) was marked by major reorganizations of the climate system, ocean circulation, and sedimentation patterns[1]. This interval began with the *Middle Miocene Climate Transition* (~14.8–13.0 Ma), when global cooling and expansion of the Antarctic Ice Sheet enhanced deep-water formation and reshaped thermohaline circulation[2,3]. Continued late Miocene cooling and oceanographic reconfiguration, including intensified deep-ocean ventilation and increased nutrient supply[4], culminated in the *Late Miocene Biogenic Bloom* (LMBB, ~8–5 Ma), a period of elevated marine productivity[1,5].

Throughout this transition, the gradual restriction and reconfiguration of ocean gateways, including the *Atlantic–Mediterranean Gateway* (AMG), modulated global ocean circulation through inter-basin exchange[6]. In the Mediterranean, convergence between Africa (Nubia) and Eurasia[7] progressively restricted the AMG between ~11.6 and 7.2 Ma, confining exchange to the narrow Betic and Rifian corridors by Tortonian times and initiating *Mediterranean Outflow Water* (MOW) into the Atlantic[8-12]. Continued tectonic restriction culminated in the formation of the Mediterranean salt giant, the *Messinian Salinity Crisis* (MSC, ~5.97–5.33 Ma)[13-18]. This event generated brines far more saline than those of the modern Mediterranean, and basin-wide evaporite sequences that sequestered a substantial fraction of the global ocean's salt[13,19]. However, reconstructions of Mediterranean–Atlantic exchange based on the Mediterranean's MSC record[18] are inconsistent with seismic evidence of MOW in the Gulf of Cadiz[20] and the impacts of this extreme event on the Atlantic, and its broader consequences, remain speculative[15,17].

Here, we investigate the late Miocene evolution of MOW (Fig. 1) using two- and three-dimensional seismic data, integrated with new stratigraphic results and age constraints from International Ocean Discovery Program (IODP) Expeditions 339, 397, and 401, together with industry exploration well data (*Fig. S1*)[21–23]. During this interval, tectonic inversion of southwest Iberia[7] (Fig. 1), including the development of a foreland basin system, emplacement of the *Gulf of Cádiz Accretionary Wedge* (GCAW), reactivation of Triassic salt structures and inherited faults, and regional margin uplift, created a complex seafloor morphology that controlled sediment routing and accommodation space[12,24,25]. In this setting, we document paleomorphological and sedimentary features (Fig. 2) that record the shifting locus of persistent, energetic overflow during the MSC, reconcile the apparent contradiction between Gulf of Cádiz and Mediterranean records of Atlantic–Mediterranean exchange, and explore the potential regional and global implications of the MSC.

RESULTS

Paleo-Mediterranean overflow: seismic stratigraphy and geomorphology evidence

Six seismic units (SU1–SU6), bounded by discontinuities (D_1–D_7), are identified in the Gulf of Cádiz, western Portuguese margin, and adjacent abyssal plains (Figs. 3, 4, *5*, 6 and *S2*) between D_1 (the Basal Foredeep Unconformity, BFU, ~8.2–8.0 Ma) and D7 (the Miocene–Pliocene boundary, MPB, 5.33 Ma).

In the Algarve Basin (Fig. 1), the basal SU1 (~8.0–7.2 Ma) is characterized by low-amplitude reflections transitioning upwards into higher-amplitude, parallel-to-wavy, continuous reflections with onlap terminations against structural highs (Fig. 3A). SU2 (~7.2–6.8 Ma) displays low-amplitude tabular reflections that locally interfinger with the *Allochthonous Unit of the Gulf of Cádiz* (AUGC) and onlap onto structural highs, transitioning upward from a wedge to a tabular drape over the AUGC (Fig. 3A). SU3 (~6.8–6.4 Ma) overlies a prominent regional erosional surface (D_3) and exhibits a mounded morphology, with low-amplitude basal reflections increasing upwards in amplitude (Fig. 3A, B) and pinching out northward. SU4 (~6.4–5.97 Ma) consists of high-amplitude, laterally continuous tabular reflections incised northwestward by channels that evolve upward from wider, shallower into narrower, deeper geometries (Fig. 3A, B). SU4 is composed of internal sub-units (Fig. 3A) that migrate laterally westward and southwestward.

A major change occurs at the base of SU5 (~5.97 Ma), which overlies a regional unconformity (D_5) interpreted as an erosional surface (Figs. 3A, *S2*). SU5 is dominated by deeply incised channels (SU5a) transitioning laterally into transparent, tabular facies (Fig. 3A). Channels are strongly erosive at their base and filled by deposits with moderate-to-low amplitude reflections. Antidunes occur locally above D_5, but higher in the section, above D_{5a}, very large erosional scours (~1 km wide, ~2-3 km long, ~30 ms or 15 m deep. Fig. 4A, B) can be identified. Depositional bedforms are common within the channels (SU5b), including large compound dunes, ~0.35-0.5 km wide, ~6 km long and ~ 100 ms (or 50 m) high (Figs. 4A, C). SU6 (~5.60–5.33 Ma) marks an abrupt shift in depositional style across D_6 (Fig. 3A, C), to transparent reflections, coincident with a major lithological change (~5.60 Ma) in IODP Site U1610[23]. It comprises at least two prominent basal channelized features (at stratigraphic levels corresponding to D_{6a} and D_{6b}, Figs. 3A, C, *S2*) infilled by chaotic to discontinuous internal reflections, capped by more continuous low-amplitude reflections (Figs. 3A, C).

Outside the Algarve Basin (Gulf of Cádiz), along the southern and western Portuguese middle slopes, SU2 and SU3 (~7.2–6.4 Ma), as well as SU6 (~5.60–5.33 Ma), have seismic facies comparable to those in the Algarve Basin, whereas SU4–SU5 (~6.4–5.60 Ma) are dominated

by weak-to-transparent facies (Fig. 5). In distal lower-slope settings southwest of Portugal (Fig. 5B), SU1 is under the *Horseshoe Chaotic Unit*, but SU2–SU3 overlie it exhibiting sheeted geometries and onlap terminations (Figs. 6A, B, C). SU4 is bounded by regional erosional surfaces (D_4, ~6.4 Ma and D_5, ~5.97 Ma) correlated with those observed in the Algarve Basin, and includes large mounded drifts separated from the lower slope by a wide moat parallel to the paleo-margin (Fig. 2). Sedimentary bedforms increase in size from SU4 to SU5 (Figs. 6A, B, C, D), with the upper part (SU5b) recording the largest bedforms (~2 km wavelength and ~150/200 ms or 75-100 m high) and the highest sedimentation rates. The upper boundary of SU5 marks a discontinuity (D_6) and transition to the transparent facies of SU6 (Fig. 6).

The spatial distribution of late Messinian morphosedimentary sectors (Fig. 2) reveals a coherent system extending from proximal to abyssal domains. The *proximal sector* is dominated by channels and scour features (SU4–SU5) indicative of intense erosion. Further downslope, a *channels-and-ridges sector* developed, where SU5 erosive channels are controlled by structural relief and locally incise underlying SU2–SU4 deposits (Figs. 2, 3). Two principal channel systems (northern and southern) are present (Fig. 2), with lengths of ~190 and ~205 km respectively, narrowing and shallowing downcurrent (proximal: ~4-5 km wide, ~70 ms or 35 m deep; distal: ~2.5-3.0 km wide and ~50 ms or 25 m deep). Channel architecture varies by orientation: alongslope channels exhibit pronounced lateral migration associated with *moat-drift systems (drifts: 5 to 10 km wide; moats: ~1 km wide),* whereas downslope channels are vertically stacked without adjacent drifts (Figs. 2, 3). Farther downflow, a *distal* or *depositional sector* is characterized by elongated, separated mounded drifts of SU4–SU5 (~50 km long, ~35 km wide, ~500 ms or 250 m thick) and associated moats (~8 km wide and 75 km long), reflecting contourite deposition from the northern channel outlet (Fig. 2). More distal areas comprise plastered and sheeted drifts (~105 km long, ~30-35 km wide), locally intersected by submarine canyons (Fig. 2). The southern channel is directly connected to the *Horseshoe Abyssal Plain* (Fig. 2), where a high-amplitude, laterally continuous, seismic unit occurs. Overall, the Messinian record documents a progressive across-slope migration of both erosional and depositional features, reflecting increasing current energy and downflow expansion of the contourite depositional system (CDS) from slope to abyssal domains (Fig. 2).

DISCUSION

Modern Mediterranean overflow: a partial analogue

As it descends, the present-day MOW (Fig. 7), evolves from a turbulent overflow into a bottom-attached, gravity-driven current, undergoing progressive mixing and lateral

spreading[26-28]. Flow velocities exceed 2–3 m s^{-1} near the sill before decreasing downslope, reaching ~1 m s^{-1} within 2 m of the seafloor ~100 km downflow of the gateway controlling sill, the Camarinal Sill[27]. Interaction between near-bottom flow and seafloor morphology (Fig. 7) generates a range of erosional and depositional features[29,30]. Farther downstream, the flow becomes increasingly geostrophic and detaches from the seabed at ~1400 m depth, forming eddies and promoting lateral dispersion in the North Atlantic, contributing significantly to the formation of *North Atlantic Deep Water* and the *Atlantic Meridional Overturning Circulation (AMOC)*[31-35].

Morphosedimentary features associated with the modern MOW (Fig. 7) provide a basis for interpreting the late Messinian record described above (Fig. 2). In particular, the development of erosional and depositional features reflects variations in flow velocity, overflow density contrast, and interaction with slope morphology. For the late Messinian, however, the location, dimensions and evolution of the geometry and persistence of the AMG remain contensted[11,15,36]. Evidence of pre-MSC MOW along the Iberian margin prior to ~6.4 Ma has been documented[11,12,20], and studies of younger Pliocene and Quaternary systems in this region demonstrate that Mediterranean overflow has generated extensive erosional surfaces and contourite deposits that migrated progressively downflow through time[30,37]. By analogy, the transition observed in our results, from drift-dominated deposits (SU2–SU3) followed by incised channels and large-scale bedforms (SU5), is consistent with the development and evolution of a dynamic overflow system. However, while pre- and post-MSC analogues provide a process-based framework for interpreting the nature and evolution of Mediterranean–Atlantic exchange during the MSC, there are clear differences in scale, geometry, and distribution of the overflow-related seismic facies between them.

Implications of Mediterranean–Atlantic exchange during the late Messinian

Seismic-stratigraphic and geomorphological evidence, including the absence of levees, overbank deposits, and terraces, as well as the lack of a clear channel–lobe transition zone, together with distinctive internal architectural elements, distinguishes the identified late Messinian features from classical turbiditic channels. In particular, the transition from alongslope to downslope channel stacking patterns, along with variations in channel hierarchy and evolutionary style, highlights their deviation from standard turbiditic models[38,39]. Sedimentological evidence supports this interpretation: high-amplitude seismic anomalies within SU4 and SU5, previously attributed to Guadalquivir Sands turbidites[12,40-42], are complemented by drilling results from IODP Site U1610 (Fig. 3A), which reveal interbedded turbidites, debrites, contourites, and bottom-current-reworked deposits[24]. This association

indicates hybrid flow behaviour, combining dense overflow and gravity-driven processes within a structurally confined foreland basin[12,25].

The late Tortonian to Messinian sedimentary record of the Algarve Basin and the southwest of Portugal margin documents an extreme, short-lived reorganization of the interaction between the Atlantic and Mediterranean overflow (Fig. 8). SU1-SU3 seismic facies indicate the development of contouritic drifts along the middle slope between ~8.2–8.0 Ma and ~6.4 Ma. These deposits reflect a relatively weak paleo–MOW, and their termination was previously interpreted as the result of its severe weakening or cessation of the outflow around ~6.4 Ma[12,20], contradicting Mediterranean MSC records, which require continuous, albeit restricted, exchange until ~5.56 Ma[18,43].

Several studies have proposed that during the Tortonian-Messinian times, the Betic-Rifian corridors, and possibly the Gibraltar corridor, were conduits for Mediterranean–Atlantic exchange[8,17,18,36] until closure of the Betic and Rifian corridors at ~7.1 Ma and ~6.8 Ma, respectively[8,18]. Two-way exchange through the Gibraltar corridor has therefore been hypothesized for the remainder of the Messinian[36]. Notably, there is no evidence for a substantial Messinian overflow trough comparable to the modern system at the Atlantic exit of the Strait of Gibraltar[12]. This suggests that either exchange operated under markedly different geometrical and hydrodynamic conditions, while not excluding shallow Atlantic inflow and/or that location of the gateway during the Messinian was not through the Gibraltar Strait.

Neither the proposed cessation of outflow at 6.4 Ma nor the location of the gateway at Gibraltar is consistent with the morphosedimentary sectors identified here (Fig. 2), which, together with SU4 to SU6 (~6.4-5.33 Ma), extend across the continental slope from the Guadalquivir Basin to the Algarve Basin and closely resemble the modern MOW system reoriented to an outflow location north of the Gibraltar Strait (Fig. 7). These features indicate a paleo-overflow that, as today, splits into distinct cores controlled by seafloor morphology, density contrasts, and Coriolis-forced deflection[26,27]. They also demonstrate that, following weak overflow and middle-slope drift-deposition (SU1–SU3), outflow did not cease at ~6.4 Ma[12], but instead transitioned to a denser and more focused downslope overflow (SU4) that penetrated to greater depths (Figs. 2, 8). The overflow became a bottom-attached gravity current by ~5.97 Ma (SU5a), which reached peak energy between ~5.78 and 5.60 Ma (SU5b, generating deeply incised channels, extensive erosional surfaces, and large sedimentary bedforms), collapsed at ~5.60 Ma, underwent subsequent intermittent reactivation until ~5.55 Ma (SU6), then ceased entirely until the MPB.

The scale of erosion, presence of vertically-stacked downslope channels, occurrence of antidunes in SU5a, and large compound dunes in SU5b (Fig. 4) imply exceptionally high

bottom shear stresses and flow velocities exceeding those of the modern MOW[27]. Compound dunes (SU5b) within the channels in the channel and ridges sector indicate boundary layer velocities of 2.3-5 m s^{-1} (maxima 6-7 m s^{-1}) in a flow ~15-20 m thick, densities of ~1030-1100 kg m^{-3} and salt concentrations of ~47-135 g kg^{-1}. Sediment waves in SU5b drifts in the depositional sector, indicate high flow velocities of 1.3-4.2 m s^{-1}, densities up to 1029-1050 kg m^{-3}, and salinities of ~40–70 g kg^{-1}. Smaller antidunes on SU5a indicate lower flow velocities (0.8–2.5 m s^{-1}), supporting increasing flow strength from SU5a to SU5b. These trends are consistent with the evolving long-term salinity structure of the Mediterranean (Fig. 8) before and during MSC Stage 1 gypsum deposition (~5.97-5.6 Ma) and Stage 2 halite formation (~5.6–5.54 Ma)[18,44].

Increasing outflow salinity would have progressively enhanced density contrasts with the wider North Atlantic, promoting faster and more coherent overflow, and driving downslope migration of the system during SU4 and SU5 deposition. Under such hypersaline conditions, the overflow likely amplified density contrasts, suppressed mixing, and promoted sediment-laden bottom-attached gravity currents, once bottom shear stress exceeded a threshold, sediment entrainment would have further increased flow density. The Messinian flow thus likely functioned as a coupled, intermittent overflow–turbidity current system, capable of reshaping continental slopes and abyssal plains over relatively short timescales.

The abrupt transition at ~5.60 Ma (D_6) to the transparent seismic facies at the base of SU6 in the Gulf of Cádiz, Portuguese margin, and adjacent abyssal plains reflects rapid collapse of this energetic system (Fig. 8), preceding the MPB and the Zanclean reflooding[45]. The shift is coeval with the Mediterranean's Intra-Messinian Unconformity (IMU), likely marking near complete cessation of Mediterranean–Atlantic exchange. Within SU6 (Fig. 3A, C) up to D_{6b} (~5.55 Ma), isolated channelized features may indicate episodic overflow reactivation and intermittent connectivity (*Fig. S2; D_6-D_7*), but between 5.55 and 5.33 Ma, a condensed succession of tabular hemipelagic deposits indicates persistent low-energy conditions. Mediterranean-Atlantic reconnection through the Strait of Gibraltar at ~5.33 Ma[33,34], initiated two-layer exchange, establishing the modern MOW and CDS along the Iberian margin[34] (Fig. 7, 8).

Tectonically, progressive AMG restriction was linked to African-Eurasian convergence and the development of the Guadalquivir foreland–Algarve foredeep basins[7]. Flexural subsidence associated with Betic–Rif orogeny and the GCAW development[25] created accommodation space for deep-marine sedimentation[12,41,42]. Closure and reorganization of the Betic and Rifian corridors also modified overflow pathways (Fig. 8), though precise paleogeography and timings remain difficult to constrain due to onshore uplift and erosion[18]. Overflow dynamics

were further modulated by active tectonics, paleobathymetric change, and climatic forcing (Fig. 8). Messinian discontinuities identified here align with younger ones at ~4.5 and ~2.4 Ma[37], denoting tectonic pulses of ~2.0/2.5 Ma duration tied to compressive-flexural stress cycles (Fig. 8), while seismic unit stacking patterns indicates ~0.4 Ma cyclicity linked to eccentricity, superimposed on tectonic pulses associated with uplift of the Gibraltar Arc[12,14]. These controls governed proximal-to-distal migration of Messinian depositional systems and the overflow intermittent behaviour, consistent with variability observed in both Tortonian and Pliocene–Quaternary records[12,40-42,46].

Our results presented here indicate that the Mediterranean overflow became sufficiently dense to descend to abyssal depths (~4000 m), with implications extending beyond regional sedimentation (Figs. 2, 8) to a reorganization of global deep-water circulation. Injection of high salinity waters into the deep Atlantic would have increased abyssal density, strengthened bottom currents, and modified pressure gradients and circulation pathways, with high-salinity MOW potentially replacing *Antarctic Bottom Water* locally as the deepest watermass in the eastern Atlantic. Whether enhanced MOW strengthened or weakened the AMOC farther afield would have depended on several factors, including the vertical profile of hypersaline MOW detrainment[47] and its influence on the trans-Atlantic density gradients governing overturning[48]. We suggest this phase of intensified, denser MOW overflow reinforced Atlantic overturning, coinciding with late Miocene cooling, stronger *Iceland–Scotland Overflow Water*, a rapid expansion of *Northern Component Water*, and enhanced AMOC between ~6.0 and 5.55 Ma[49]. In contrast, the final decline of the MOW at ~5.55 Ma coincided with a transition to warmer climatic conditions[4], and weakening AMOC[49], suggesting a diminished MOW contribution to North Atlantic circulation. The absence of an intermediate-depth paleo–MOW between 6.4 and ~5.55 Ma may have allowed Arctic- and Antarctic-sourced intermediate waters[28] to expand, promoting cooling, ventilation, and late Messinian surface-water cooling[4]. This cooling phase coincided with changes along the Antarctic margins compatible with fully glacially dominated margin conditions[50], and development of ephemeral Northern Hemisphere ice sheets[1]. This period also coincided with enhanced eastern boundary and equatorial upwelling systems[6], which may have influenced nutrient cycling during the LMBB. Although the biogenic bloom likely reflects multiple drivers[1,5], enhanced bottom-water formation and circulation could have promoted nutrient redistribution and intensified upwelling, while turbulent mixing along topographic barriers may have injected nutrients into intermediate waters. Late Miocene gateway-controlled overflow may therefore have had local, regional and global influence (Fig. 8).

In summary, this work establishes the first Atlantic evidence of Mediterranean–Atlantic exchange, documenting sustained, deep-reaching Mediterranean overflow into the Atlantic

from 6.4- 5.55 Ma. Mediterranean overflow is a key oceanographic response to gateway evolution: plate-tectonic activity and the restriction or opening of oceanic gateways can rapidly reorganize deep-ocean water-mass structure and circulation, reshaping upwelling, nutrient redistribution, deep-water sedimentation, and thermohaline circulation. These reorganizations can occur over remarkably short geological timescales, underscoring the sensitivity of deep-ocean circulation to tectonically driven changes in gateway geometry. Further collaborative research integrating (paleo)oceanography, marine geology, geophysics, paleoclimatology and numerical modelling is essential to disentangle the influence of ancient overflows and gateways on ocean circulation and Earth's climatic and biogeochemical evolution.

MATERIALS AND METHODS

The main objective of this study is to identify evidence for Messinian paleo-overflow of Mediterranean waters into the Atlantic Ocean and to improve our understanding of Mediterranean–Atlantic gateway exchange before, during, and after the Messinian Salinity Crisis (MSC). We focus on the region downstream of the Strait of Gibraltar, encompassing the Gulf of Cádiz and the western Portuguese margin. This study integrates new data from the Atlantic margin to reconstruct late Miocene paleomorphology, based on an extensive network of 2D and 3D seismic datasets with sediment cores recovered from *Integrated Ocean Drilling Program and International Ocean Discovery Program* (IODP) Expeditions 339, 397, and 401[21-23], together with data from ten industry wells (*Fig. S1*), all of which provide robust chronostratigraphic constraints. IODP Expedition 401 (10 December 2023–9 February 2024) constituted the offshore drilling component of the *Land-to-Sea* scientific drilling proposal "Investigating Miocene Mediterranean–Atlantic Gateway Exchange" (IMMAGE). The Late Miocene sedimentary record was analysed in detail and correlated across the Gulf of Cádiz, the western Portuguese margin, and adjacent abyssal plains (*Fig. S1*).

The Messinian age control is based on astronomically calibrated bioevents[51, 52-55], whereas Pliocene age control is based on planktonic foraminifera bioevents[56]. The resulting chronostratigraphic framework integrates age constraints from IODP Expeditions 339, 397, and 401[21-23], together with regional stratigraphic interpretations[11, 12, 20, 37]. In addition, Sierro et al. [57] recently conducted a cyclostratigraphic analysis of the industry well logs throughout the Messinian and Pliocene, enabling tuning to an astronomical target and the construction of a high-resolution age model. This framework was essential for constraining the ages of key discontinuities (D) and seismic units (SU) in this study.

Acquisition of downhole logging data during IODP Expedition 401 was limited. The absence of vertical seismic profiling (VSP) and checkshots, together with borehole inclination

constraints, prevented accurate core–downhole–seismic integration during the drilling expedition. During post-expedition research, these limitations were subsequently addressed through detailed correlation of 15 wells, including IODP Expedition 339 Sites U1386 and U1387, with the regional seismic framework (*Fig. S1*). A total of 14 regionally correlatable horizons spanning the last 8.2 My were identified across the wells. The IODP 339 sites provide critical constraints on the Messinian–Pliocene boundary (MPB), as well as the Pliocene and Quaternary intervals. The remaining 13 industry wells (Algarve-2; Atlántida-2 and -3; Gulf of Cádiz B-2, B-3, B-6, C-2, C-3, C-4, D-1, D-4, E-1, and 6-x-1, *Fig. S1*) were key for estimating reference ages for the Tortonian and Messinian intervals. Among the 14 horizons, eight are considered as robust age markers based on reliable bioevents or well constrains regional stratigraphic horizons[11,12, 25, 34, 37, 40-42, 58-60]: 3.57 Ma (IPD= intra Pliocene discontinuity); 3.8 and 4.52 Ma (EPD= early Pliocene discontinuity); 5.33 Ma (MPB/M= Miocene–Pliocene boundary); 6.08 Ma; 6.34 Ma; <6.95 Ma; and 8.0–8.2 Ma (BFU= Basal Foredeep Unconformity). The remaining six horizons are less constrains compared with the previous ones but useful for a regional correlation: 0.4 Ma (LQD= late Quaternary discontinuity); 0.7 Ma (MPD= mid Pleistocene discontinuity); 2.2–2.4 Ma (EQD= early Quaternary discontinuity); 3.0–3.2 Ma (LPD= late Pliocene discontinuity); 5.4/5.6 Ma (IMU= Intra-Messinian Unconformity); and <7.24 Ma (Top Gulf of Cádiz Accretionary Wedge, GCAW). These horizons were regionally correlated across the seismic dataset and tied to IODP Expedition 401 Site U1610A. Subsequently, two-way travel times (TWT) were calculated for each horizon, allowing the generation of a synthetic checkshot file for depth-to-time conversion.

The 3D seismic data from the Algarve Basin was interpreted based on established seismic stratigraphic principles[65,66] to map key discontinuities (D) and seismic units (SU). Advanced seismic interpretation workflows implemented in the *PaleoScan* software were used to extract stratigraphic information and identify geomorphological elements. Semi-automatic 3D seismic interpretation generated horizon patches linked within a relative chronostratigraphic framework, from which an effectively unlimited number of chronostratigraphic surfaces can be extracted and mapped with various attributes highlighting the spatio-temporal evolution of the system. High resolution colour processing (eXchroma) provided a color attribute which corresponds to the average lithology with a vertical resolution of approximately 5 m[67]. The method uses an approach similar to multi-spectral satellite-image processing, whereby three adjacent time or depth slices from a seismic data cube are combined and enhanced through RGB colour processing and structural sharpening. Repetition of this process in the vertical direction of the 3D seismic cube produces a structurally sharpened RGB (SRGB) cube. Colour images extracted along interpreted seismic horizons from the SRGB cube form the basis of the visualizations presented in *Fig. S2*.

Large sedimentary dunes occur in the upper part of SU5 (SU5b) in both proximal and distal sectors (Figs. 2, 3, and 5). Bedform geometry and spatial patterns derived from seismic data and PaleoScan analyses were used to estimate the main characteristics of the parent flow and the sediment composition of the bedforms. Scaling relationships based on bedform wavelength, height, and sediment composition were applied to estimate boundary-layer thickness and dominant sediment grain size[68,69]. Independent constraints derived from the densimetric-Froude phase diagram for dense-flow bedforms, bedform steepness (height-to-wavelength ratio), the Shields parameter[69], and friction coefficients estimated from boundary-layer properties[70] support the interpretation of vigorous bottom currents generated by relatively dense saline overflows, likely intensified by topographic confinement and local slope gradients. An iterative calculation procedure was developed to ensure the consistency and robustness of the predictions. Boundary-layer thickness was first estimated from bedform wavelength, considering the characteristic scaling relationships between wavelength and lower dense boundary-layer height (approximately 5–10× for dunes and 15–30× for antidunes, depending on sediment grain size). Bedform type (i.e., dune or antidune) and sediment characteristics were then used to derive ranges of total flow resistance, expressed as friction coefficients. These coefficients account for both skin friction and form drag in the case of dunes, whereas only skin friction was considered for antidunes. Subsequently, Shields parameters were estimated using the phase-space regions corresponding to each bedform type[69], which in turn provided estimates of flow velocity. The calculations were iteratively refined until consistency was achieved among the densimetric Froude number, the predicted bedform phase, and the Shields diagram evaluated for the characteristic sediment grain size. This procedure yielded final estimates of the average flow velocity and density within the lower dense boundary layer.

The values presented on this work for flow velocity, density, and salinity, estimated for the large compound dunes (SU5b) within the channels of the channel-and-ridge sector, were obtained considering Shields parameters ranging from 1 to 3 (for sediment sizes ranging from 0.3–0.5 mm), while total friction coefficients (including skin and form drag) range from 0.001 to 0.003, with $b \sim 0.15$-0.2 corresponding to the fractional contribution of the upper boundary layer relative to bed friction. Estimated densimetric Froude numbers for these dunes ranged between 1.5 and 2.5. The equivalent values for the antidunes in the depositional sector, over the drifts in S5b, were likewise calculated considering Shields parameters ranging from 0.8 to 2 (0.04 mm for flocculated mud to 0.1 mm). Estimated friction coefficients are lower (0.0008–0.001), consistent with limited flow separation across the bedforms. Although flow density was likely reduced due to overspill above the channel/moat floor and mixing down-channel, the formation of these large-scale antidunes was probably promoted by a still fairly

dense lower layer and by steeper topographic gradients along the transition from drift crest to flank. Densimetric Froude numbers for these antidunes ranged from 1.4 to 1.6.

References

1. Steinthorsdottir, M. et al. The Miocene: the future of the past. *Paleoceanogr. Paleoclimatol.* **36**, e2020PA004037. https://doi.org/10.1029/2020PA004037 (2021).
2. Leutert, T. J., Auderset, A., Martínez-García, A., Modestou, S. & Meckler, A. N. Coupled Southern Ocean cooling and Antarctic ice sheet expansion during the middle Miocene. *Nat. Geosci.* **13**, 634–639 https://doi.org/10.1038/s41561-020-0623-0 (2020).
3. Westerhold, T. et al. An astronomically dated record of Earth's climate and its predictability over the last 66 million years. *Science* **369**, 1383–1387 https://doi.org/10.1126/science.aba6853 (2020).
4. Herbert, T. D. et al. Late Miocene global cooling and the rise of modern ecosystems. *Nat. Geosci.* **9**, 843–847 https://doi.org/10.1038/ngeo2813 (2016).
5. Pillot, Q., Suchéras-Marx, B., Sarr, A.-C., Bolton, C.T. & Donnadieu, Y. A global reassessment of the spatial and temporal expression of the Late Miocene Biogenic Bloom. *Paleoceanogr. Paleoclimatol.* **38**, e2022PA004564 https://doi.org/10.1029/2022PA004564 (2023).
6. Hernández-Molina, F. J. & Scotese, C. R. Mesozoic and Cenozoic oceanic gateway evolution and global tectonics: paleoceanographic and sedimentary implications, in *Oceanic Gateways: Modern and Ancient Analogues and their Conceptual and Economic Implications*, Hernández-Molina, F. J., Davoli, G., Stirling, E. J., Chiarella, D. & Viana, A. R., Eds., Geological Society, London, Special Publications **553** gslspecpub2025-10. https://doi.org/10.1144/gslspecpub2025-10 (2026).
7. Vergés, J. & Fernández, M. Tethys–Atlantic interaction along the Iberia–Africa plate boundary: the Betic–Rif orogenic system. *Tectonophysics* **579**, 144–172. https://doi.org/10.1016/j.tecto.2012.08.032 (2012).
8. Martín, J. M., Puga-Bernabéu, Á., Aguirre, J. & Braga, J. C. Miocene Atlantic–Mediterranean seaways in the Betic Cordillera (southern Spain). *Rev. Soc. Geol. Esp.* **27**, 175–186 http://hdl.handle.net/10481/42694 (2014).
9. Capella, W. et al. Mediterranean isolation preconditioning the Earth System for late Miocene climate cooling. *Sci. Rep.* **9**, 3795 https://doi.org/10.1038/s41598-019-40208-2 (2019).
10. de Weger, W. et al. Contourite depositional system after the exit of a strait: case study from the late Miocene South Rifian Corridor, Morocco. *Sedimentology* **68**, 2996–3032 https://doi.org/10.1111/sed.12882 (2021).
11. Ng, Z. L. et al. Late Miocene contourite depositional system of the Gulf of Cádiz: the sedimentary signature of the paleo-Mediterranean Outflow Water. *Mar. Geol.* **442**, 106605 https://doi.org/10.1016/j.margeo.2021.106605 (2021).
12. Ng, Z. L. et al. Late Miocene evolution of the eastern Deep Algarve basin: interaction of bottom currents and gravitational processes in a foredeep setting. *Mar. Pet. Geol.* **141**, 105695 https://doi.org/10.1016/j.marpetgeo.2022.105695 (2022).
13. Hsü, K. J., Ryan, W. B. & Cita, M. B. Late Miocene desiccation of the Mediterranean. *Nature* **242**, 240–244 https://doi.org/10.1038/242240a0 (1973).

14. Krijgsman, W., Hilgen, F., Raffi, I., Sierro, F. J. & Wilson, D. S. Chronology, causes and progression of the Messinian salinity crisis. *Nature* **400**, 652–655 https://doi.org/10.1038/23231 (1999).

15. Krijgsman, W. et al. Causes and consequences of the Messinian salinity crisis. *Nat. Rev. Earth Environ.* **5**, 335–350 https://doi.org/10.1038/s43017-024-00533-1 (2024).

16. Roveri, M. et al. The Messinian salinity crisis: past and future of a great challenge for marine sciences. *Mar. Geol.* **352**, 25–58 https://doi.org/10.1016/j.margeo.2014.02.002 (2014).

17. Roveri, M., Lugli, S. & Manzi, V. The desiccation and catastrophic refilling of the Mediterranean: 50 years of facts, hypotheses, and myths around the Messinian salinity crisis. *Annu. Rev. Mar. Sci.* **17**, 485–509 https://doi.org/10.1146/annurev-marine-021723-110155 (2025)

18. Flecker, R. et al. Evolution of the Late Miocene Mediterranean–Atlantic gateways and their impact on regional and global environmental change. *Earth-Sci. Rev.* **150**, 365–392 https://doi.org/10.1016/j.earscirev.2015.08.007 (2015).

19. Haq, B., Gorini, C., Baur, J., Moneron, J., & Rubino, J.-L. Deep Mediterranean's Messinian evaporite giant: how much salt? *Glob. Planet. Change* **184**, 103052 https://doi.org/10.1016/j.gloplacha.2019.103052 (2020).

20. Ng, Z. L. et al. Manar, Latest Miocene restriction of the Mediterranean Outflow Water: a perspective from the Gulf of Cádiz. *Geo-Mar. Lett.* **41**, 23 https://doi.org/10.1007/s00367-021-00693-9 (2021).

21. Stow, D. A. V., Hernández-Molina, F. J., Alvarez Zarikian, C. A. & the Expedition 339 Scientists, *Mediterranean Outflow*, Proceedings of the Integrated Ocean Drilling Program vol. 339 (Integrated Ocean Drilling Program Management International, Tokyo). https://doi.org/10.2204/iodp.proc.339.2013 (2013).

22. Hodell, D. A., Abrantes, F., C. A. Alvarez Zarikian, C. A. & the Expedition 397 Scientists, *Iberian Margin Paleoclimate*, Proceedings of the International Ocean Discovery Program vol. 397 (International Ocean Discovery Program). https://doi.org/10.14379/iodp.proc.397.101.2024 (2024).

23. Flecker, R., Ducassou, E., Williams, T. & the Expedition 401 Scientists, *Mediterranean–Atlantic Gateway Exchange*, Proceedings of the International Ocean Discovery Program vol. 401 (International Ocean Discovery Program, College Station, TX). https://doi.org/10.14379/iodp.proc.401.2025 (2025).

24. Gutscher, M.-A. et al. Evidence for active subduction beneath Gibraltar. *Geology* **30**, 1071 https://doi.org/10.1130/0091-7613(2002)030<1071:EFASBG>2.0.CO;2 (2002).

25. Duarte, D. et al. Structural control and tectono-sedimentary evolution of the Gulf of Cadiz since the late Miocene: implications for the contourite depositional system, SW Iberia. *Mar. Geol.* **449**, 106818 https://doi.org/10.1016/j.margeo.2022.106818 (2022).

26. Baringer, M. O. & Price, J. F. Mixing and spreading of the Mediterranean outflow. *J. Phys. Oceanogr.* **27**, 1654–1677 https://doi.org/10.1175/1520-0485(1997)027<1654:MASOTM>2.0.CO;2 (1997).

27. Sánchez-Leal, R. F. et al. The Mediterranean Outflow in the Gulf of Cádiz: a rough journey. *Sci. Adv.* **3**, 11 https://doi.org/10.1126/sciadv.aao0609 (2017).

28. Roque, D., Parras-Berrocal, I., Bruno, M., Sánchez-Leal, R. F. & Hernández-Molina, F. J. Seasonal variability of intermediate water masses in the Gulf of Cadiz: implications of the Antarctic and Subarctic seesaw. *Ocean Sci.* **15**, 1381–1397 https://doi.org/10.5194/os-15-1381-2019 (2019).

29. Hernández-Molina, F. J. et al. Looking for clues to paleoceanographic imprints: a diagnosis of the Gulf of Cadiz contourite depositional systems. *Geology* **31**, 19–22 https://doi.org/10.1130/0091-7613(2003)031%3C0019:LFCTPI%3E2.0.CO;2 (2003).

30. Llave, E. et al. Reconstructions of the Mediterranean Outflow Water during the Quaternary since the study of changes in buried mounded drift stacking pattern in the Gulf of Cadiz. *Mar. Geophys. Res.* **28**, 379–394 https://doi.org/10.1007/s11001-007-9040-7 (2007).

31. Morozov, E. G., Filyushkin, B. N. & Velarde, M. G. Contribution of Mediterranean Water to the formation of North Atlantic Deep Water. *Eur. Phys. J. Spec. Top.* https://doi.org/10.1140/epjs/s11734-025-01993-2 (2025).

32. Reid, J. L. On the contribution of the Mediterranean Sea outflow to the Norwegian-Greenland Sea. *Deep Sea Res. A* **26**, 1199–1223 https://doi.org/10.1016/0198-0149(79)90064-5 (1979).

33. Rogerson, M., Rohling, E. J., Bigg, G. R. & Ramirez, J. Paleoceanography of the Atlantic-Mediterranean exchange: overview and first quantitative assessment of climatic forcing. *Rev. Geophys.* **50**, RG2003 https://doi.org/10.1029/2011RG000376 (2012).

34. Hernández-Molina, F. J. et al. Onset of Mediterranean outflow into the North Atlantic. *Science* **344**, 1244–1250 https://doi.org/10.1126/science.1251306 (2014).

35. Calvo, E., Malanotte-Rizzoli, P., Menna, M., Martellucci, R. & Zambianchi, E. Mediterranean outflow waters supply North Atlantic convection sites. *Nat. Commun.* https://doi.org/10.1038/s41467-026-75523-6 (2026).

36. Krijgsman, W. et al. Gibraltar Corridor: watergate of the Messinian Salinity Crisis. *Mar. Geol.* **403**, 238–246 https://doi.org/10.1016/j.margeo.2018.06.008 (2018).

37. Hernández-Molina, F. J. et al. Evolution of the Gulf of Cadiz margin and Southwest Portugal contourite depositional system: tectonic, sedimentary and paleoceanographic implications from IODP Expedition 339. *Mar. Geol.* **377**, 7–39 https://doi.org/10.1016/j.margeo.2015.09.013 (2016).

38. Hodgson, D. M. & Dunn, R. J. H. Submarine slope systems: processes, products and controls on their evolution, in *Submarine Slope Systems: Processes and Products*, S. S. Flint, D. M. Hodgson, Eds., Geological Society, London, Special Publications **418** pp. 1–35. (2016).

39. de Leeuw, J., Eggenhuisen, J. T. & Cartigny, M. J. B. Linking submarine channel–levee facies and architecture to flow structure of turbidity currents: insights from flume tank experiments. *Sedimentology* **65**, 931–951 https://doi.org/10.1111/sed.12411 (2018).

40. Riaza, C. & Martínez del Olmo, W. Depositional model of the Guadalquivir–Gulf of Cadiz Tertiary basin, in *Tertiary Basins of Spain: The Stratigraphic Record of Crustal Kinematics*, P. F. Friend, C. J. Dabrio, Eds., World and Regional Geology **6** (Cambridge Univ. Press, Cambridge), pp. 330–338. https://doi.org/10.1017/CBO9780511524851.047 (1996).

41. Sierro, F. J., González-Delgado, J. A., Dabrio, C. J., Flores, J. A. & Civis, J. Late Neogene depositional sequences in the foreland basin of Guadalquivir (SW Spain), in *Tertiary Basins of Spain: The Stratigraphic Record of Crustal Kinematics*, Friend, P. F. & Dabrio, C. J. Eds., World and Regional Geology **6** (Cambridge Univ. Press, Cambridge), pp. 339–345. https://doi.org/10.1017/CBO9780511524851.048 (1996).

42. Ledesma, S. M. Astrobiocronología y estratigrafía de alta resolución del Neógeno de la Cuenca del Guadalquivir-Golfo de Cádiz. Thesis, Universidad de Salamanca, Salamanca http://oceano.usal.es/wp-content/uploads/sites/30/2017/10/SantiagoLedesmaTesis.compressed-1.pdf (2000).

43. Aloisi, G. et al. Chlorine isotopes constrain a major drawdown of the Mediterranean Sea during the Messinian salinity crisis. *Nat. Commun.* **15**, 9671 https://doi.org/10.1038/s41467-024-53781-6 (2024).
44. Vasiliev, I. et al. Large sea surface temperature, salinity, and productivity-preservation changes preceding the onset of the Messinian Salinity Crisis in the Eastern Mediterranean Sea. *Paleoceanogr. Paleoclimatol.* **34**, 182–202 https://doi.org/10.1029/2018PA003438 (2019).
45. Garcia-Castellanos, D. et al. The Zanclean megaflood of the Mediterranean—searching for independent evidence. *Earth-Sci. Rev.* **201**, 103061 https://doi.org/10.1016/j.earscirev.2019.103061 (2020).
46. de Weger, W. et al., Late Miocene contourite channel system reveals intermittent overflow behavior. *Geology* **48**, 1194–1199 https://doi.org/10.1130/G47944.1 (2020).
47. McDougall, T. J., Holmes, R. M. & Gunn, K. L. What sets the bulk stratification in the abyss? *J. Phys. Oceanogr.* **55**, 2079–2095 https://doi.org/10.1175/JPO-D-24-0180.1 (2025).
48. Roquet, F. et al. Controls of the global overturning circulation of the ocean. *npj Clim. Atmos. Sci.* **8**, 304 https://doi.org/10.1038/s41612-025-01185-8 (2025).
49. Karatsolis, B.-T. Evolution of deep-water circulation in the North-East Atlantic during the latest Miocene warming. *EGUsphere* [Preprint] https://doi.org/10.5194/egusphere-2026-3764 (2026).
50. Zachos, J. C., Pagani, M., Sloan, L., Thomas, E. & Billups, K. Trends, rhythms, and aberrations in global climate 65 Ma to present. *Science* **292**, 686–693 https://doi.org/10.1126/science.1059412 (2001).
51. Sierro, F. J., Flores, J. A., Civis, J., González Delgado, J. A. & Francés, G. Late Miocene globorotaliid event-stratigraphy and biogeography in the NE-Atlantic and Mediterranean. *Mar. Micropaleontol.* **21** https://doi.org/10.1016/0377-8398(93)90013-N (1993).
52. Hilgen, F. J. & Krijgsman, W. Cyclostratigraphy and astrochronology of the Tripoli diatomite formation (pre-evaporite Messinian, Sicily, Italy). *Terra Nova* **11**, 16–22 https://doi.org/10.1046/j.1365-3121.1999.00221.x (1999).
53. Lirer, F. et al., Mediterranean Neogene planktonic foraminifer biozonation and biochronology. *Earth-Sci. Rev.* **196** https://doi.org/10.1016/j.earscirev.2019.05.013 (2019).
54. Raffi, I. et al., The Neogene Period, in *Geologic Time Scale 2020*, Gradstein, F. M., Ogg, J. G., Schmitz, M. D. & Ogg, G. M. Eds. (Elsevier), pp. 1141–1215. https://doi.org/10.1016/B978-0-12-824360-2.00029-2 (2020).
55. Bulian, F., Jiménez-Espejo, F. J., Andersen, N., Larrasoaña, J. C. & Sierro, F. J. Mediterranean water in the Atlantic Iberian margin reveals early isolation events during the Messinian Salinity Crisis. *Glob. Planet. Change* **231**, 104297 https://doi.org/10.1016/j.gloplacha.2023.104297 (2023).
56. Sierro, F. J., Ledesma, S., Flores, J.-A., Torrescusa, S., Martinez del Olmo, W. Sonic and gamma-ray astrochronology: cycle-to-cycle calibration of Atlantic climatic records to Mediterranean sapropels and astronomical oscillations. *Geology* **28**, 695–698 https://doi.org/10.1130/0091-7613(2000)28<695:SAGACT>2.0.CO;2 (2000).
57. Sierro, F. J. et al. Seven Million Years of Mediterranean Evolution Shaped by Atlantic Atmospheric Forcing and Gibraltar Arc Tectonics (submitted).

58. Maldonado, A., Somoza, L., Pallarés, L. The Betic orogen and the Iberian–African boundary in the Gulf of Cádiz: geological evolution (central North Atlantic). *Mar. Geol.* **155**, 9–43 https://doi.org/10.1016/S0025-3227(98)00139-X (1999).

59. Roque, C. et al. Pliocene and Quaternary depositional model of the Algarve margin contourite drifts (Gulf of Cadiz, SW Iberia): seismic architecture, tectonic control and paleoceanographic insights. *Mar. Geol.* **303**, 42–62 https://doi.org/10.1016/j.margeo.2011.11.001 (2012).

60. Hernández-Molina, F. J. et al. Contourite processes associated with the Mediterranean Outflow Water after its exit from the Strait of Gibraltar: global and conceptual implications. *Geology* **42**, 227–230 https://doi.org/10.1130/G35083.1 (2014).

61. Cohen, K., Harper, D., Gibbard, P. & Car, N. The ICS International Chronostratigraphic Chart this decade. *Episodes* **48**, 105–115 https://doi.org/10.18814/epiiugs/2025/025001 (2025).

62. Haq, B. U. & Ogg, J. G. Retraversing the highs and lows of Cenozoic sea levels. *GSA Today* **34**, 4–11 https://doi.org/10.1130/GSATGG593A.1 (2024).

63. Laskar, J., Robutel, P., Joutel, F., Gastineau, M., Correia, A. C. M. & Levrard, B. A long-term numerical solution for the insolation quantities of the Earth. *Astron. Astrophys.* **428**, 261–285 https://doi.org/10.1051/0004-6361:20041335 (2004).

64. Lanterna, F., Krijgsman, W., Lourens, L., Mulch, A. & Vasiliev, I. Sea surface temperature and salinity changes in the easternmost Mediterranean during the pre-evaporitic Messinian controlled by the restriction at Gibraltar. *Paleoceanogr. Paleoclimatol.* **41**, e2025PA005277 https://doi:10.1029/2025PA005277 (2026).

65. Mitchum Jr., R. M., Vail, P. R. & Sangree, J. B. Seismic stratigraphy and global changes of sea level, part 6: stratigraphic interpretation of seismic reflection patterns in depositional sequences, in *Seismic Stratigraphy—Applications to Hydrocarbon Exploration*, C. E. Payton, Ed., AAPG Memoir 26 (American Association of Petroleum Geologists), pp. 117–133 (1977).

66. Catuneanu, O. et al. Towards the standardization of sequence stratigraphy. *Earth-Sci. Rev.* **92**, 1–33 https://doi:10.1016/j.earscirev.2008.10.003 (2009).

67. Laake, A. Structural interpretation in color—a new RGB processing application for seismic data. *Interpretation* **3**, SC1–SC8 https://doi.org/10.1190/INT-2014-0041.1 (2015).

68. Fedele, J. J. Bedforms and gravity underflows in marine environments. Thesis, University of Illinois, Urbana-Champaign, 402 p. (2002).

69. Fedele, J. J., Hoyal, D., Barnaal, Z., Tulenko, J. & Awalt, S. Bedforms created by gravity flows, in *Autogenic Dynamics and Self-Organization in Sedimentary Systems*, Budd, D. A., Hajek, E. A., & Purkis, S. J. Eds., SEPM Special Publication 106 (SEPM Society for Sedimentary Geology) https://doi.org/10.2110/sepmsp.106 (2016).

70. American Society of Civil Engineers, Garcia, M. H. Ed., *Sedimentation Engineering: Processes, Measurements, Modeling, and Practice*, ASCE Manuals and Reports on Engineering Practice No. 110, ASCE (2007).

71. Medialdea, T. et al. Structure and evolution of the "olistostrome" complex of the Gibraltar Arc in the Gulf of Cádiz (eastern Central Atlantic): evidence from two long seismic cross-sections. *Mar. Geol.* **209**, 173–198 https://doi.org/10.1016/j.margeo.2004.05.029 (2004).

72. Duarte, J. C. et al. Thrust–wrench interference tectonics in the Gulf of Cadiz (Africa–Iberia plate boundary in the North-East Atlantic): insights from analog models. *Mar. Geol.* **289**, 135–149 https://doi.org/10.1016/j.margeo.2011.09.014 (2011).

73. Ramos, A., Fernández, O., Muñoz, J. A. & Terrinha, P. Impact of basin structure and evaporite distribution on salt tectonics in the Algarve Basin, Southwest Iberian margin. *Mar. Pet. Geol.* **88**, 961–984 https://doi.org/10.1016/j.marpetgeo.2017.09.028 (2017).

74. Neves, M. C., Terrinha, P., Afilhado, A., Moulin, M., Matias, L. & Rosas, F. Response of a multi-domain continental margin to compression: study from seismic reflection–refraction and numerical modelling in the Tagus Abyssal Plain. *Tectonophysics* **468**, 113–130 https://doi.org/10.1016/j.tecto.2008.05.008 (2009).

75. Gamboa, D., Omira, R., Piedade, A., Terrinha, P., Roque, C. & Zitellini, N. Destructive episodes and morphological rejuvenation during the lifecycles of tectonically active seamounts: insights from the Gorringe Bank in the NE Atlantic. *Earth Planet. Sci. Lett.* **559**, 116772 https://doi.org/10.1016/j.epsl.2021.116772 (2021).

76. Morozov, E. G., Filyushkin, B. N., & Velarde, M. G. Contribution of Mediterranean Water to the formation of North Atlantic Deep Water. *Eur. Phys. J. Spec. Top.* https://doi.org/10.1140/epjs/s11734-025-01993-2 (2025).

77. Swingedouw, D., Colin, C., Eynaud, F., Ayache, M., & Zaragosi, S. Impact of freshwater release in the Mediterranean Sea on the North Atlantic climate. *Clim. Dyn.* **53**, 3893–3915 https://doi:10.1007/s00382-019-04758-5 (2019).

78. Lugli, S., Manzi, V., Roveri, M., Schreiber, B. C. The Primary Lower Gypsum in the Mediterranean: a new facies interpretation for the first stage of the Messinian salinity crisis. *Palaeogeogr. Palaeoclimatol. Palaeoecol.* **297**, 83–99 https://doi.org/10.1016/j.palaeo.2010.07.017 (2010).

79. Andreetto, F. et al. High-amplitude water-level fluctuations at the end of the Mediterranean Messinian salinity crisis: implications for gypsum formation, connectivity and global climate. *Earth Planet. Sci. Lett.* **595**, 117767 https://doi.org/10.1016/j.epsl.2022.117767 (2022).

80. García-Castellanos, D., Heida, H., Palcu, D. V., Bulian, F. & Sierro, F. Kilometric sea level changes during the Messinian salinity crisis caused by river erosion and climate. *Sci. Adv.* **11**, eads9752 https://doi.org/10.1126/sciadv.ads9752 (2025).

Acknowledgments: This study was conducted within the framework of the IMMAGE project, "The Drifters" Research Group, and linked to the ALGEMAR (PID2021-123825OB-I00, MICIU/AEI/10.13039/501100011033) and DRIFT (PID2025-175838NB-I00) projects. Sediment cores and associated shipboard data were collected during IODP Expedition 401 aboard the JOIDES Resolution. Seismic data were provided by Repsol S.A., TGS-Nopec, and the Direção Geral de Energia e Geologia (DGEG), Portugal, subjected to confidentiality restrictions. We thank Romain Pellen (IFREMER - GM-LGS, France) for the late Messinian paleogeographic reconstruction background in Figure 2. We thank M. Bruno (Univ. Cádiz, Spain), R. F. Sánchez-Leal (IEO, Spain), and D. Roque (KAUST, Saudi Arabia) for the stimulating discussions that greatly contributed to our understanding of the modern oceanographic processes in the Gulf of Cádiz.

Funding:

Land-to-Sea scientific drilling "Investigating Miocene Mediterranean–Atlantic Gateway Exchange" (IMMAGE Project): HM, FS, FR, SY, MT, ELL, SL, ED, TW, RF.

International Ocean Discovery Program (IODP) Expedition 401, 10 December 2023 to 9 February 2024.

(https://iodp.tamu.edu/scienceops/expeditions/mediterranean_atlantic_gateway_exchange.html), ICDP-2018/09; IODP Proposal 895 / Expedition 401: HM, FS, FR, SY, MT, ED, TW, RF.

"The Drifters" Research Group: HM, DD, ZLN, SY, MT, ELL.

ALGEMAR project, MCIN/AEI (PID2021-123825OB-I00, MICIU/AEI/10.13039/501100011033): ELL, HM, FS, DD, ZLN, SL, RM, AA, ED, RF.

DRIFT project, MCIN/AEI (PID2025-175838NB-I00): HM, FS, AL, DD, ZLN, SY, MT, CS, ELL, RM, AA, ED.

Author contributions:

Initials: F.J. Hernández-Molina (HM), F.J. Sierro (FS), A. Laake (AL), D. Duarte (DD), Z.L. Ng (ZLN), F. Raad (FR), S. Yin (SY), M. Teixeira (MT), C. Serie (CS), E. Llave (ELL), S. Ledesma (SL), J. Fedele (JF), A. Naveira-Garabato (ANG), A. Piola (AP), M. Ron Martin (RM), A. Arnaiz (AA), E. Ducassou (ED), T. Williams (TW), R. Flecker (RF)

Conceptualization: HM, FS, DD, ZLN

Funding acquisition: RF, ED, HM, ELL

Investigation: HM, FS

Methodology: HM, AL, FR, CS, JF, DD, ZLN, SY

Project administration: RF, ED, TW, HM

Resources: HM, RM, AA, ELL

Software: HM, AL, DD, ZLN, SY

Supervision: HM, FS

Validation: HM, AL, FR, CS, JF, DD, SY

Discussion: HM, FS, AL, DD, ZLN, FR, SY, MT, CS, ELL, SL, JF, ANG, AP, RM, AA, ED, TW, RF

Visualization: HM, AL, CS

Writing – original draft: HM

Writing – review & editing: HM, FS, AL, DD, ZLN, FR, SY, MT, CS, ELL, SL, JF, ANG, AP, RM, AA, ED, TW, RF

Competing interests: Authors declare that they have no competing interests.

Materials & correspondence: correspondence and material request to F. Javier Hernánadez-Molina (fj.h@csic.es). All data and materials used in this analysis from the IODP Expedition 401 data is publicly accessible through: a) The Expedition 401 Proceedings volume: https://publications.iodp.org/proceedings/401/401title.html, b) The IODP LIMS Report Interface (LORE): web.iodp.tamu.edu/LORE, and c) "Access Data and Samples" portal (IODP.org), and the Site Survey Data Bank:

https://www.iodp.org/resources/access-data-and-samples. Industry well data can be available through: a) the MITECO map of hydrocarbon borehole locations, permits, and concessions (https://www.miteco.gob.es/en/energia/hidrocarburos-nuevos-combustibles/petroleo/exploracion/map-sondeos.html), Ministerio para la Transición Ecológica y el Reto Demográfico; and (b) the IGME (Instituto Geológico y Minero de España) Hydrocarbon Database (https://info.igme.es/catalogo/resource.aspx?portal=1&catalog=3&ctt=1&lang=spa&resource=47). 2D and 3D seismic datasets were provided by Repsol S.A., TGS-NOPEC, and the Direção-Geral de Energia e Geologia (DGEG), Portugal, and are subject to confidentiality restrictions. These datasets are archived at the Andalusian Earth Sciences Institute (IACT), Spanish National Research Council (CSIC), Granada, Spain.

FIGURES

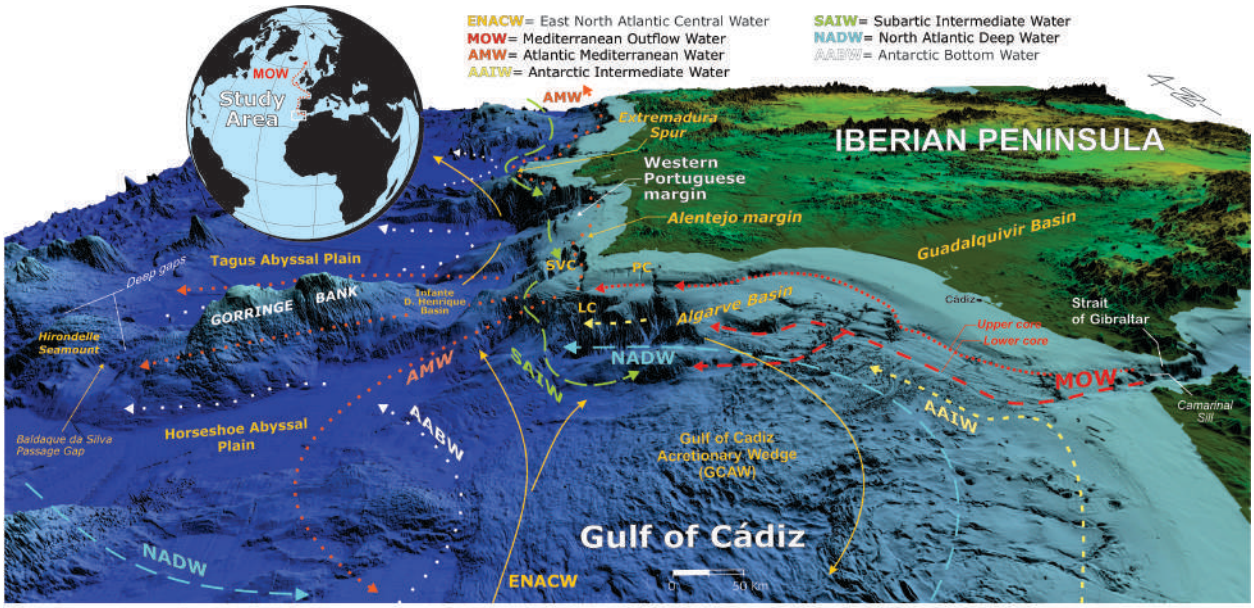

Figure 1

Figure 1. Study area with the regional present day water masses circulation including the modern Mediterranean Outflow Water (MOW).

Next page

Figure 2. Late Messinian paleogeographic reconstruction and the distribution of the main morphosedimentary sectors (1 to 4) and segments of the paleo-overflow of Mediterranean Water into the Atlantic (*onshore reconstruction within the Guadalquivir Basin based on Ledesma, 2000*[42]). Sectors 5 and 6 correspond to Horseshoe and Tagus abyssal plains. Abbreviations (*in alphabetic order*): AA= Afonso de Albuquerque Seamount, AGDH= Albufeira-Guadalquivir-Doñana High, AH= Alentejo High, CB= Cádiz Basin, CC= Cascais canyon, CF=Cádiz Fault, DB= Doñana Basin, FC= Faro Canyon, GB= Guadalquivir Bank, GDR= Guadalquivir Diapiric Ridge, GEFZ= Gil Eanes Fault Zone, HCU= Horseshoe Chaotic Unit, LC= Lagos Canyon, MP= Marquês de Pombal Plateau, PC= Portimão Canyon, SB= Sanlúcar Basin, SC= Setubal Canyon, SP= Sines Plateau, SVC= São Vicente Canyon.

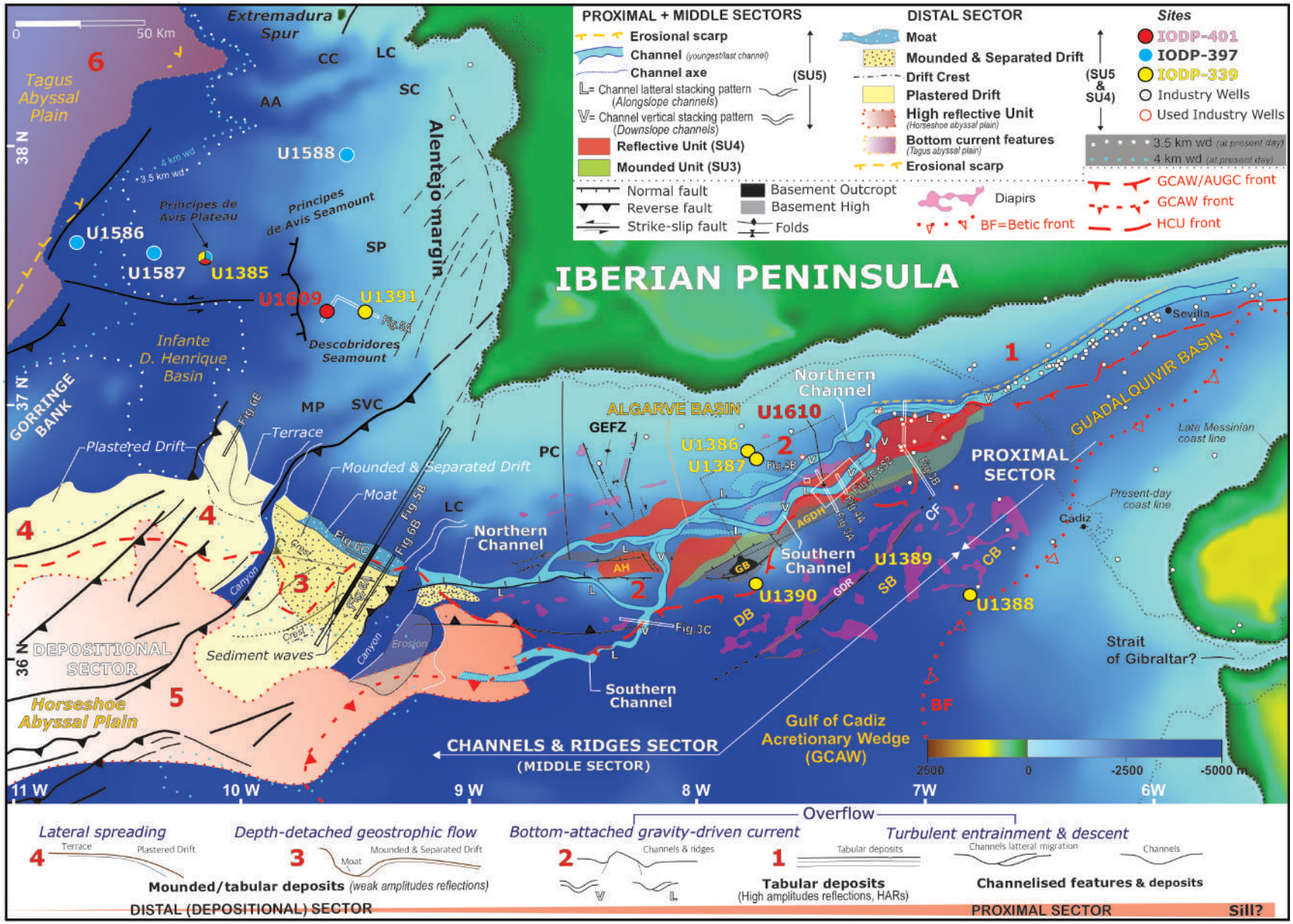
PROXIMAL + MIDDLE SECTORS
Erosional scarp
Channel (youngest/last channel)
Channel axe
L= Channel latteral stacking pattern (Alongslope channels)
V= Channel vertical stacking pattern (Downslope channels)
Reflective Unit (SU4)
Mounded Unit (SU3)
(SU5)
DISTAL SECTOR
Moat
Mounded & Separated Drift
Drift Crest
Plastered Drift
High reflective Unit (Horseshoe abyssal plain)
Bottom current features (Tagus abyssal plain)
Erosional scarp
(SU5 & SU4)
Sites
IODP-401
IODP-397
IODP-339
Industry Wells
Used Industry Wells
3.5 km wd (at present day)
4 km wd (at present day)
Normal fault
Reverse fault
Strike-slip fault
Basement Outcropt
Basement High
Folds
Diapirs
BF=Betic front
GCAW/AUGC front
GCAW front
HCU front
IBERIAN PENINSULA
Extremadura Spur
Tagus Abyssal Plain
Alentejo margin
Principes de Avis Plateau
Principes de Avis Seamount
Descobridores Seamount
Infante D. Henrique Basin
GORRINGE BANK
Plastered Drift
Terrace
Mounded & Separated Drift
Moat
Sediment waves
DEPOSITIONAL SECTOR
Horseshoe Abyssal Plain
ALGARVE BASIN
Northern Channel
Southern Channel
PROXIMAL SECTOR
GUADALQUIVIR BASIN
Late Messinian coast line
Present-day coast line
Strait of Gibraltar?
Gulf of Cadiz Acretionary Wedge (GCAW)
CHANNELS & RIDGES SECTOR
(MIDDLE SECTOR)
U1588
U1586
U1587
U1385
U1609
U1391
U1610
U1386
U1387
U1389
U1390
U1388
Sevilla
Cadiz
Overflow
Lateral spreading
Depth-detached geostrophic flow
Bottom-attached gravity-driven current
Turbulent entrainment & descent
Mounded/tabular deposits (weak amplitudes reflections)
Tabular deposits (High amplitudes reflections, HARs)
Channelised features & deposits
DISTAL (DEPOSITIONAL) SECTOR
PROXIMAL SECTOR
Sill?

Figure 2

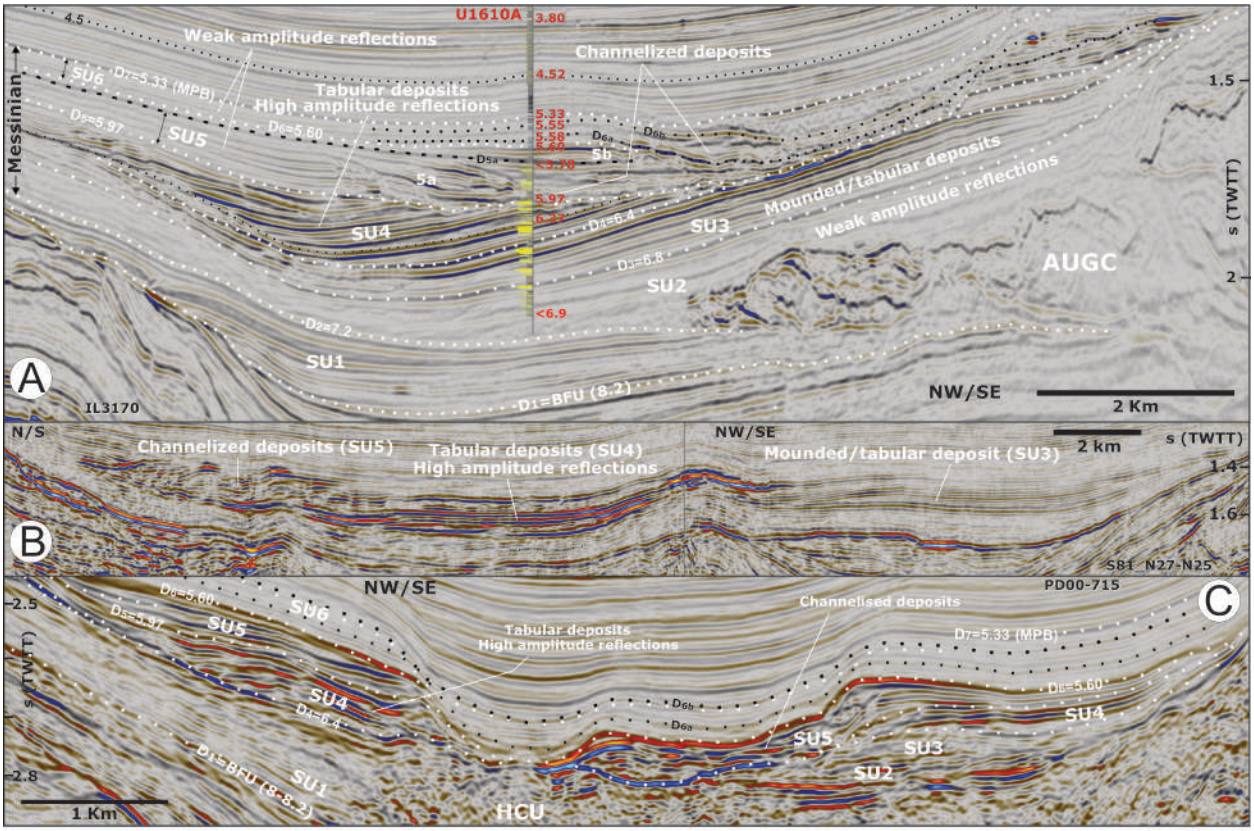

Figure 3

Figure 3. Late Messinian erosional and depositional features within the channel-and-ridges sector of the Algarve Basin, including seismic units (SU), discontinuities (D, white dotted), and selected key horizons (black dashed): A) general seismic-unit stacking pattern, lithology, and key ages from IODP Expedition 401, Site U161025; B) proximal sector showing the seismic characteristics of SU3, SU4, and SU5; and C) late Messinian erosional and depositional features within the distal channel-and-ridges sector. Location shown in Figs. 2 and *S1*.

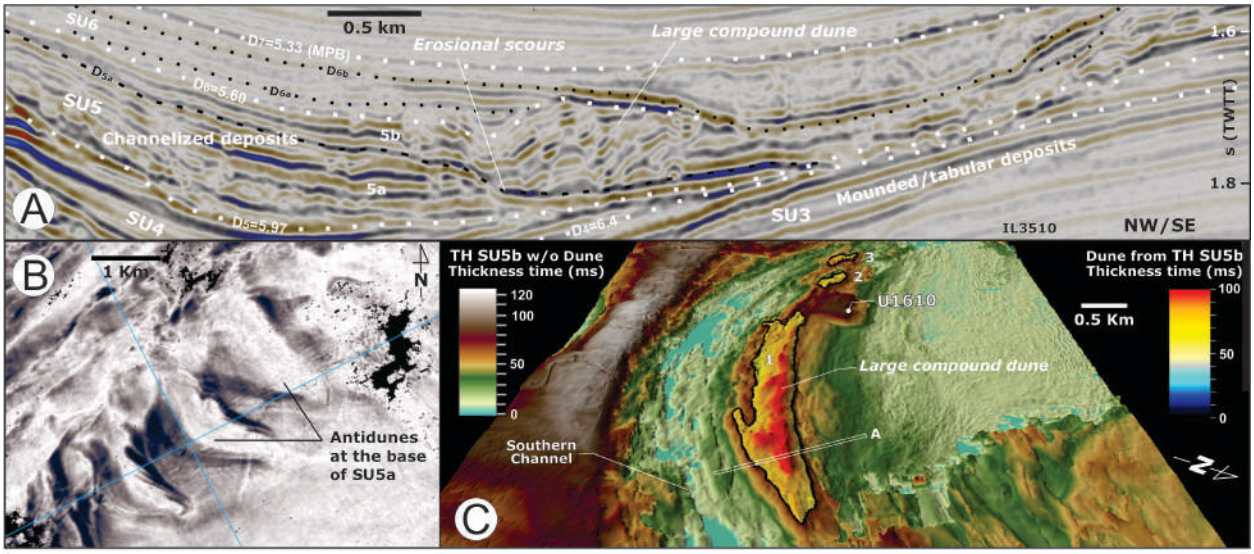

Figure 4

Figure 4. Large dunes within SU5 in the channel-and-ridges sector: A) large compound dunes within SU5b. Ages are indicated in Ma; B) RMS GeoBlend PaleoScan highlighting the seismic geomorphology, including examples of antidunes at the base of SU5a overlying D5; C) large compound dunes within SU5b overlying large erosional scours shown in A, with dune-body thickness (m) highlighted using a blue-to-red colour scale. The background thickness map of the SU5b interval is shown using a topographic colour scale. Location shown in Figs. 2 and *S1*; location of panel A is indicated in C.

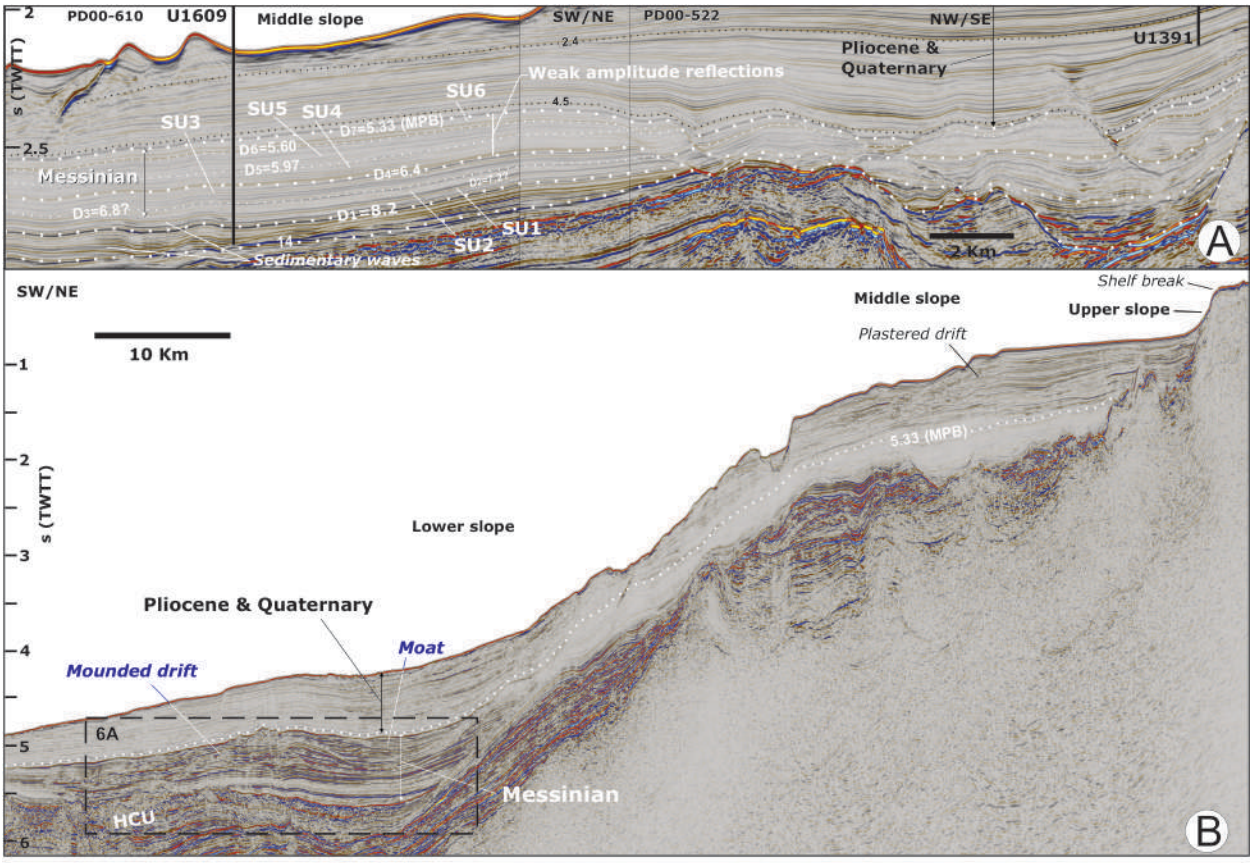

Figure 5. Late Messinian erosional and depositional features, including seismic units (SU), discontinuities (D, white dotted), and selected key horizons (black dashed), in the western (A) and southern (B) Portuguese middle and lower slopes. Outside the Algarve Basin, along the southern and western Portuguese middle slopes, SU4–SU5 are dominated by sheeted, weak-to-transparent seismic facies. Nevertheless, in the distal part of the lower slope, they display higher-amplitude seismic facies and include large mounded drifts separated from the lower slope by a wide moat parallel to the palaeo-margin. Location shown in Figs. 2 and *S1*.

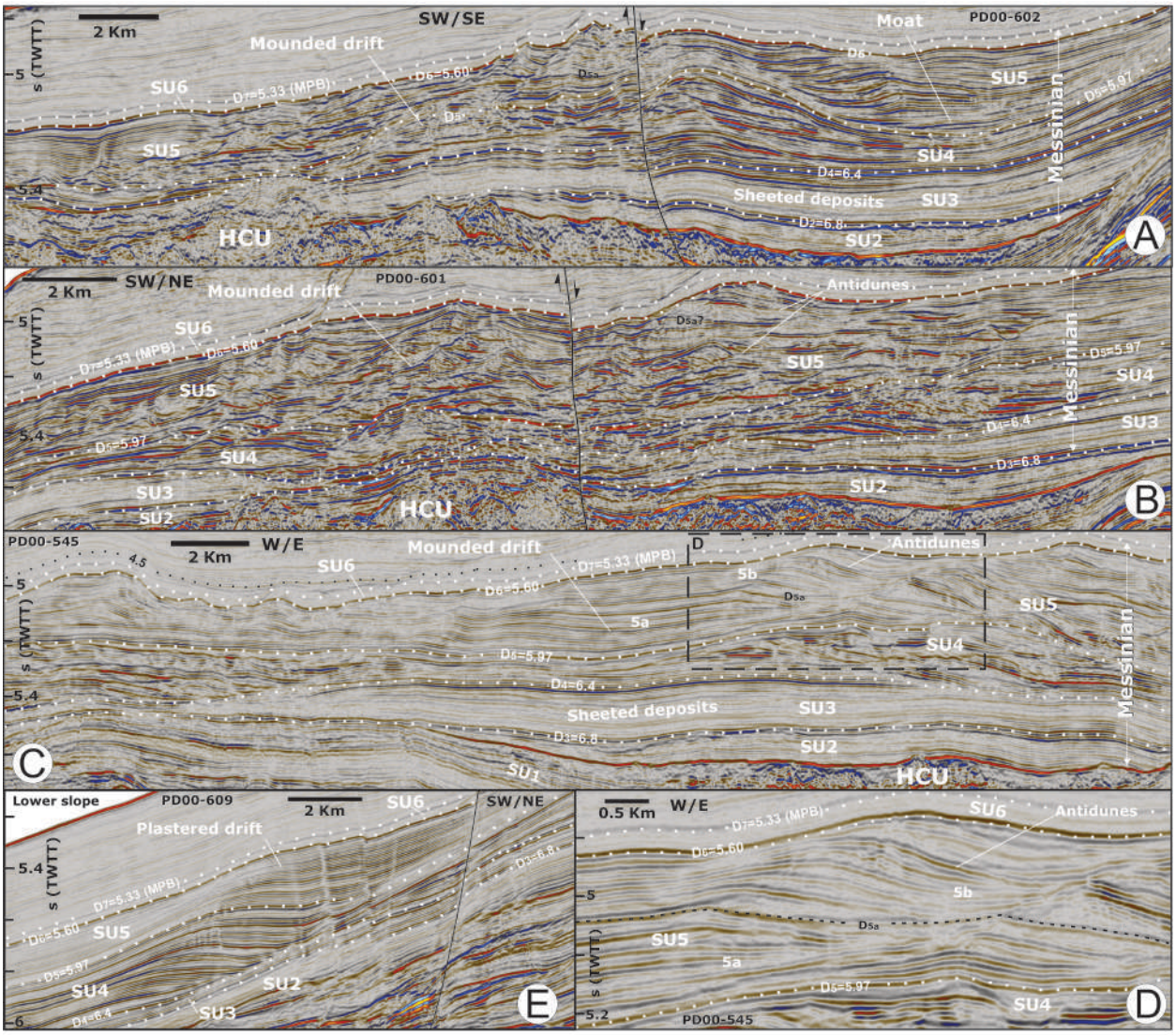

Figure 6

Figure 6. Distal depositional sector, including seismic units (SU), discontinuities (D, white dotted), and selected key horizons (black dashed): A–C) large contourite mounded drifts and sedimentary waves (antidunes); D) detail of large antidunes within SU5b; and E) plastered drifts within the distal sector along the southern Portuguese lower continental slope. Abbreviation: HCU, Horseshoe Chaotic Unit. Ages are indicated in Ma. Locations of panels A–E are shown in Figs. 2 and *S1*; location of panel D is shown in C.

Next Page

Figure 7. Modern Mediterranean overflow, including its principal flow segments, interactions with seafloor irregularities and major morphosedimentary sectors (simplified and adapted from Hernández-Molina et al.[29]). Abbreviations (*in alphabetic order*): AA= Afonso de Albuquerque Seamount, AGDH= Albufeira-Guadalquivir-Doñana High, AH= Alentejo High, CB= Cádiz Basin, CC= Cascais canyon, CF=Cádiz Fault, DB= Doñana Basin, FC= Faro Canyon, GB= Guadalquivir Bank, GDR= Guadalquivir Diapiric Ridge, GEFZ= Gil Eanes Fault Zone, HCU= Horseshoe Chaotic Unit, LC= Lagos Canyon, MP= Marquês de Pombal Plateau, PC= Portimão Canyon, SB= Sanlúcar Basin, SC= Setubal Canyon, SP= Sines Plateau, SVC= São Vicente Canyon.

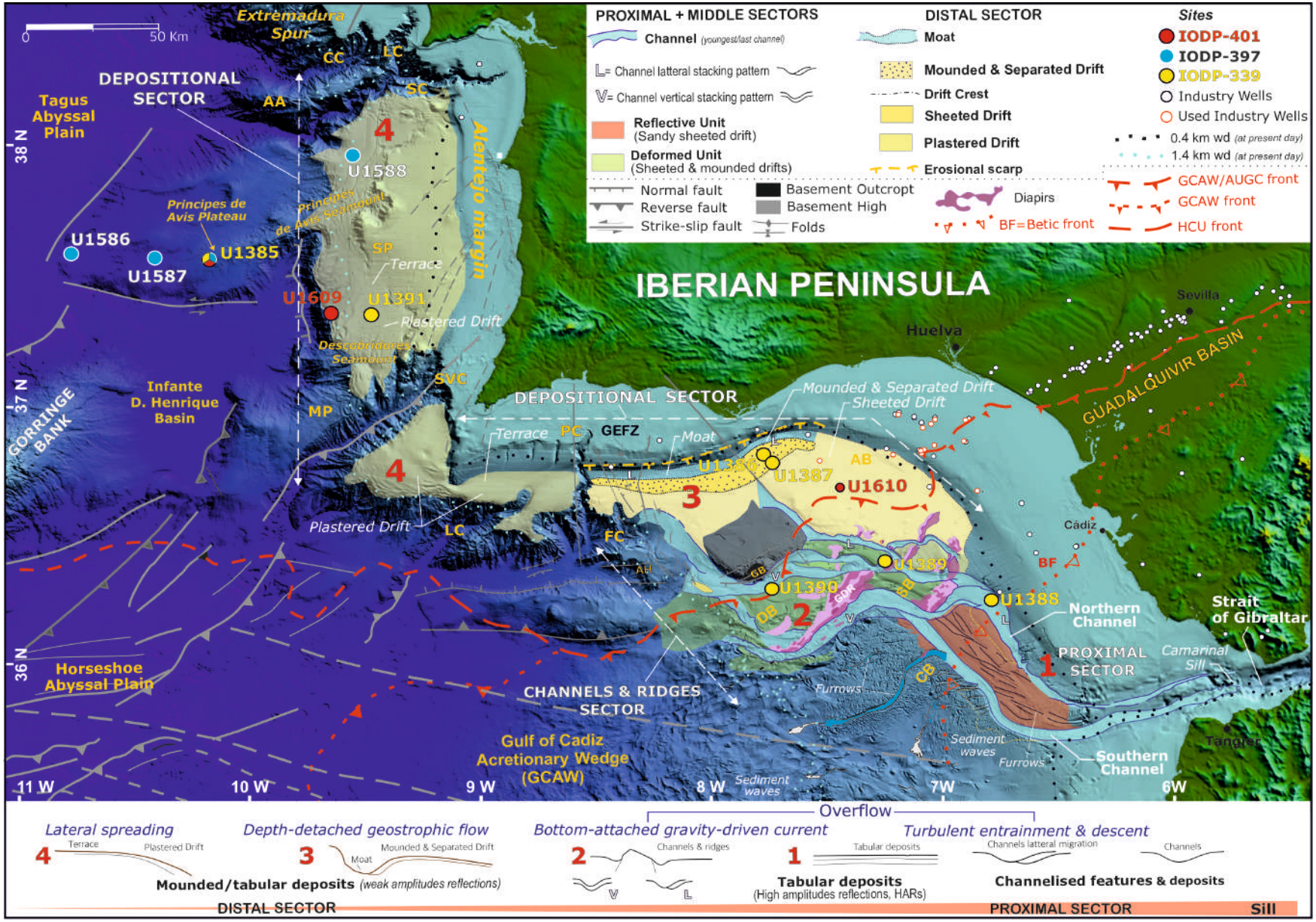
PROXIMAL + MIDDLE SECTORS
Channel (youngest/last channel)
L= Channel latteral stacking pattern
V= Channel vertical stacking pattern
Reflective Unit (Sandy sheeted drift)
Deformed Unit (Sheeted & mounded drifts)
Normal fault
Reverse fault
Strike-slip fault
Basement Outcropt
Basement High
Folds
DISTAL SECTOR
Moat
Mounded & Separated Drift
Drift Crest
Sheeted Drift
Plastered Drift
Erosional scarp
Diapirs
BF=Betic front
Sites
IODP-401
IODP-397
IODP-339
Industry Wells
Used Industry Wells
0.4 km wd (at present day)
1.4 km wd (at present day)
GCAW/AUGC front
GCAW front
HCU front
IBERIAN PENINSULA
Extremadura Spur
DEPOSITIONAL SECTOR
Tagus Abyssal Plain
Alentejo margin
Principes de Avis Plateau
Principes de Avis Seamount
Descobridores Seamount
Infante D. Henrique Basin
GORRINGE BANK
Horseshoe Abyssal Plain
Gulf of Cadiz Acretionary Wedge (GCAW)
CHANNELS & RIDGES SECTOR
PROXIMAL SECTOR
GUADALQUIVIR BASIN
Sevilla
Huelva
Cádiz
Northern Channel
Strait of Gibraltar
Camarinal Sill
Southern Channel
Tangier
Furrows
Sediment waves
Terrace
Plastered Drift
Moat
Mounded & Separated Drift
Sheeted Drift
GEFZ
U1385
U1386
U1587
U1588
U1609
U1391
U1387
U1610
U1389
U1390
U1388
CC
LC
SC
AA
SP
SVC
MP
PC
FC
AB
GB
DB
CB
BF
4
3
2
1
38 N
37 N
36 N
11 W
10 W
9 W
8 W
7W
6W
0
50 Km
Lateral spreading
Depth-detached geostrophic flow
Bottom-attached gravity-driven current
Overflow
Turbulent entrainment & descent
Mounded/tabular deposits (weak amplitudes reflections)
Tabular deposits (High amplitudes reflections, HARs)
Channelised features & deposits
DISTAL SECTOR
PROXIMAL SECTOR
Sill

Figure 7

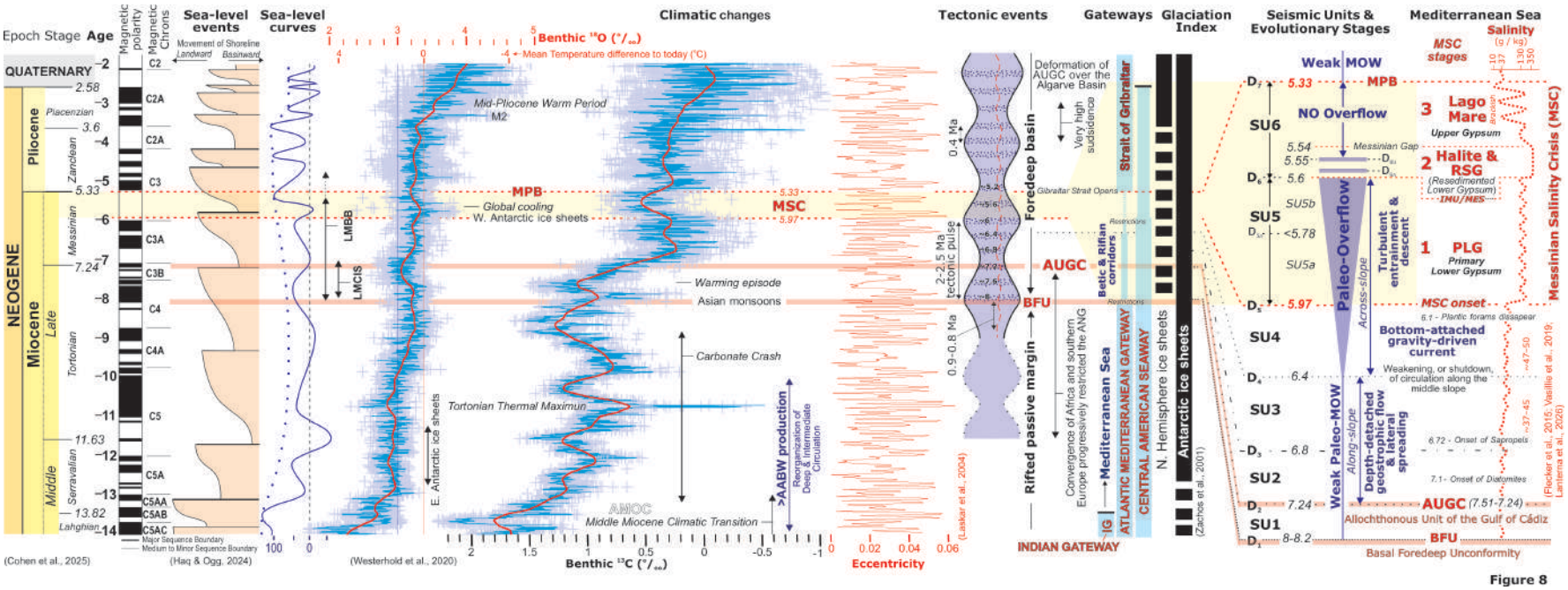

Figure 8

Figure 8. Evolution of Late Miocene overflow the Gulf of Cádiz and the western Portuguese margin, correlated to the major sea level changes[62], climatic variability[3, 63], the Glaciation Index[50], salinity variability in the Mediterranean Sea[18, 44, 64] and discussed paleoceanographic and tectonic changes. The international chronostratigraphic chart follows Cohen et al[61].

Supplementary Files

This is a list of supplementary files associated with this preprint. Click to download.

- NatureCommunicationsSupplementaryMaterialsOverflowvJavierHMII.pdf
- FigureS2final.pdf